

Terahertz plasma wave generation in ultra-short-channel Field Effect Transistors: theory vs experiment

M. V. Cheremisin, G. G. Samsonidze¹

¹*A.F.Ioffe Physical-Technical Institute, St.Petersburg, Russia*

Taking into account both the scattering and the velocity saturation of carriers, we examine the "shallow-water" instability of the two-dimensional electron gas in a field effect transistor. It is shown that both the scattering (which is analogous to friction in a shallow-water channel) and the carrier velocity saturation lead to damping of the plasma wave instability. Threshold diagram of instability is calculated. The actual device parameters required for observation of plasma wave generation are compared with those reported in recent sub-terahertz emission experiments.

PACS numbers: 72.30+q, 73.20Mf

INTRODUCTION

Recently, the interest in the plasma wave generation mechanism [1] in an ultrashort-channel Field Effect Transistor (FET) has resumed. As it was demonstrated in Ref.[1], the behavior of high-density two-dimensional electron gas (2DEG) can be described by equations analogous to the hydrodynamic equations for shallow water, the plasma waves being similar to waves in this medium. With the carrier scattering neglected, it is shown that asymmetric boundary conditions with a fixed voltage at the source and fixed current at the drain lead to an instability of steady state with a dc current. The FET channel can be regarded as a resonator, with a plasma-wave generation mechanism similar to that known for self-excitation of jets and organ pipes. Both the eigenfrequencies and the instability increment have been found for zero-dissipation electrons. In Refs.[2,3] a strongly nonlinear instability mode, in which shock waves are formed in the channel, was analyzed. In Ref.[4], the instability increment and threshold were calculated for the realistic case of nonzero carrier scattering at arbitrary currents and electron momentum relaxation times. The scattering results in the narrowing of the instability region, with the increment decreasing. The instability vanishes at a certain critical magnitude of friction. Computer simulations [4] provide a strong support for theoretical predictions. The plasma wave instability in short-channel FETs is very important for application of these devices as high-power sources and detectors in the terahertz (THz) frequency range[5]-[10](see also [11]). The sub-THz emission recently observed in short-channel FETs [12,13] was attributed to the plasma wave generation mechanism [1].

In the present paper, we analyze the plasma wave instability in the presence of both the scattering and the velocity saturation of carriers. We plot the instability diagram for device parameters required for plasma wave generation. We demonstrate that the 2DEG samples studied in [12,13] have an insufficient carrier mobility and, hence, the observed sub-THz emission cannot be understood in terms of the plasma wave generation scenario.

ANALYTICAL APPROACH

Steady state

According to Ref.[1], the high-density 2DEG in an ultra-short channel FET can be described by the following equations analogous to the hydrodynamic equations for shallow water:

$$\frac{\partial U}{\partial t} + \frac{\partial(VU)}{\partial x} = 0, \quad (1)$$

$$\frac{\partial V}{\partial t} + \frac{\partial}{\partial x} \left(\frac{V^2}{2} + \frac{eU}{m} \right) + \frac{V}{\tau} = 0. \quad (2)$$

Here, the voltage swing, $U = U_{gc} - U_T$, corresponds to a shallow water level, U_{gc} is the local gate-to-channel voltage, U_T the threshold voltage, V the local electron flux velocity, m the effective mass, and τ the momentum relaxation time due to collisions of electrons with phonons and (or) impurities. Eq.(1) is the continuity equation, in which the Shockley relation for the gradual channel approximation, $N = CU/e$, is taken into account. Here, N is the surface electron concentration, and C is the capacitance per unit area. Note that there is no direct hydrodynamic analogy for the friction term $\frac{V}{\tau}$ in the Euler equation specified by Eq.(2).

It has been shown [1] that in the absence of friction($\tau \rightarrow \infty$), which is further named the "clean limit," the steady electron flow with a constant U, V is unstable against small perturbations $\delta V, \delta U \sim \exp(-i\omega t)$ under the following boundary conditions:

$$U(0, t) = U_s, \quad U(l, t)V(l, t) = j/WC, \quad (3)$$

where U_s is the fixed source($x = 0$) potential, j the current fixed at the drain ($x = l$), and W the gate width. In the steady state, $U = U_s, V = V_s = j/(WC U_s)$. The real and imaginary parts of ω (see Figs.1, 2) are given by [1]

$$\omega'_n = \frac{S}{2l} |1 - M^2| \pi n, \quad \omega'' = \frac{S}{2l} (1 - M^2) \ln \left| \frac{1 + M}{1 - M} \right|, \quad (4)$$

where $M = V/S$ plays the role of the Mach number in hydrodynamics, $S = \sqrt{eU/m}$ is the local plasma wave velocity, and n is an odd integer for $|M| < 1$ and even integer for $|M| > 1$. Actually, the instability is related to the plasma wave amplitude enhancement caused by certain boundary reflections[1]. Two different plasma waves with wave vectors $k_{1,2} = \pm\omega/(S(1\pm M))$ propagate down- and upstream, respectively. The argument of the logarithm in Eq.(4) contains the round-trip gain factor, $(1+M)/(1-M)$, which is the product of the reflection coefficients at two boundaries. The plasma wave propagates downstream during the time, $l/(S(1+M))$, whereas the back propagation takes a longer time, $l/(S(1-M))$. When $M \rightarrow 1$, the round-trip time of the plasma wave becomes infinite, and, therefore, both the proper frequency and the instability increment vanish (see Figs.1,2).

The friction of electron flow results in a spatial dependence [14] of both the voltage and the velocity. In this case, the instability problem for small perturbations superimposed on the steady state flow V, U becomes extremely difficult. Fortunately, this problem can be solved by the high-order mode method suggested in Ref.[4]. This approach makes it possible to deduce both the instability increment and the threshold for arbitrary currents and friction strengths. As expected, the scattering leads to instability damping. At a certain critical friction, the instability vanishes.

The special interest of the present paper is in the friction term which has always been assumed to contain a constant momentum relaxation time τ previously [14,4]. We argue that the drift velocity in real 2D systems at high electric fields approaches a certain saturation value V_{sat} . In the conventional FETs just the drift velocity saturation (DVS) mechanism determines the saturation current. In order to account for the possible influence of the DVS effect on the instability, we further investigate the realistic model with the momentum relaxation time in Eq.(2) replaced as

$$\tau \rightarrow \frac{\tau}{1 + \mu E/V_{sat}}, \quad (5)$$

where μ is the low-field mobility of the 2D system, and $E = -\frac{dU}{dx}$ is the electric field. We further demonstrate that the DVS effect leads to an extra damping of the plasma wave instability.

Using Eqs.(1,2), we obtain for the steady state

$$\begin{aligned} j &= WCVU = \text{const}, \\ \frac{\partial M}{\partial \eta} &= \frac{3}{2} \frac{\gamma}{M_s^{1/3}} \frac{M^{7/3}}{\phi(M, p)}, \end{aligned} \quad (6)$$

where $\eta = x/l$ is the dimensionless coordinate, $\gamma = l/(S_s \tau)$ the friction parameter, and S_s the plasma wave velocity at the source. Then, $\phi(M, p) = 1 - M^2 - p s M$, where $s = S/S_s = (M_s/M)^{1/3}$ is the dimensionless local plasma wave velocity, and M_s is the Mach number at the

source. Then, we introduce the dimensionless parameter $p = \frac{S_s}{V_{sat}}$ associated with the DVS effect. Previous studies [14,4] correspond to the $p = 0$ case.

We are further interested only in the case of a subsonic flow case, when $0 < M \leq 1$. According to Eq.(6), at finite γ the Mach number increases from the initial value M_s at the source to some drain value $M_d = M(1)$. Note that at fixed p the increasing solution to Eq.(6) is possible when $\phi(M_s, p) > 0$ or $M_s < M_s^{\max}(p) = \sqrt{p^2/4 + 1} - p/2$. If $M_s < M_s^{\max}$, the electron flow velocity saturates at the drain, where the electric field is the strongest (i.e., $E \sim \frac{dM}{d\eta} \rightarrow \infty$), as the expression in the denominator in the right-hand part of Eq.(6) goes to zero. The Mach number at the drain cannot exceed a certain value $M_d^{\text{sat}} \leq 1$ specified by the condition $\phi(M_d, p) = 0$.

It is instructive to compare our results with those provided by the hydrodynamic "choking" saturation [14] and the conventional DVS mechanism separately. Without DVS (i.e. $p = 0$), we reproduce the "choking" criterion [14] as $M_d^{\text{sat}} = 1$. In the conventional hydrodynamics, the above condition corresponds to a subsonic gas flow which cannot evaluate to a supersonic one. In the opposite DVS case, (see, for example, Ref.[15]) the current is saturated when the condition $1 - p s M = 0$ is satisfied at the drain contact. We emphasize that both the mechanisms combined (as in Eq.(6)) result in a faster current saturation, compared with the case when each of them is considered separately.

The solution to Eq.(6) determines the steady-state spatial dependence of the Mach number $M(\eta)$:

$$f(M_s) - f(M) = \frac{2\gamma\eta}{M_s^{1/3}}, \quad (7)$$

where $f(M) = M^{-4/3} + 2M^{2/3} - 2pM_s^{1/3}M^{-2/3}$. At a fixed friction strength γ , the Mach numbers M_s and M_d are related by

$$f(M_s) - f(M_d) = \frac{2\gamma}{M_s^{1/3}}. \quad (8)$$

Substituting $M_d = M_d^{\text{sat}}$ into Eq.(8), we obtain the saturation threshold $\gamma_{\text{sat}}(M_s, p)$, represented in Fig.3 by dotted lines, for different values of the DVS parameter p . As expected, the saturation current ($\sim M_s$) at fixed γ decreases as the DVS parameter p increases.

Instability

We now study the stability of the steady-state flow by inspecting the temporal behavior of small perturbations $V_1(\eta), U_1(\eta)$ superimposed on a steady flow with a velocity $V(\eta)$ and channel potential $U(\eta)$. Thus, we take

$$\begin{aligned} V(\eta, t) &= V(\eta) + V_1(\eta) \exp(-i\omega t), \\ U(\eta, t) &= U(\eta) + U_1(\eta) \exp(-i\omega t). \end{aligned} \quad (9)$$

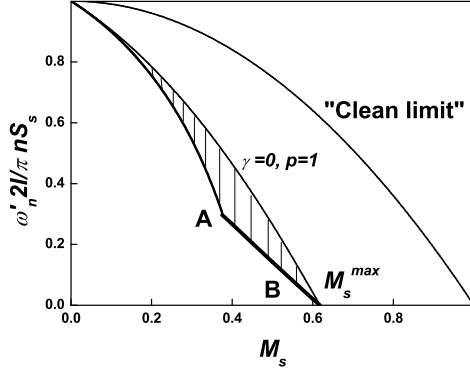


FIG. 1: Dimensionless frequency $\frac{\omega'_n 2l}{\pi n S_s}$ vs the Mach number at the source for the "clean limit" [1] at $p; \gamma = 0$. The shadowed area corresponds to that in the instability threshold diagram (see Fig.3) and shows all the frequencies that can be generated ($\omega'' > 0$) at fixed $p = 1$ and $0 < \gamma < 0.32$. The bold line A-B shows the frequency $\omega'(M_s)$ in the saturation mode (see the corresponding line in Fig.3). The point B corresponds to $M_s^{max}(1) = 0.62$.

Equations (1),(2),(3), linearized with respect to V_1 and U_1 , yield:

$$\begin{aligned} -i\Omega\gamma v_1 + \frac{d}{d\eta}(v_0 v_1 + u_1) - p(v_1 u'_0 + v_0 u'_1) + \gamma v_1 &= 0, \\ -i\Omega\gamma u_1 + \frac{d}{d\eta}(u_0 v_1 + u_1 v_0) &= 0. \\ u_0(0) = 0, u_0(1)v_1(1) + u_1(1)v_0(1) &= 0 \end{aligned} \quad (10)$$

where $v_1 = V_1/S_s$, $v_0 = V(\eta)/S_s$, $u_1 = U_1/U_s$, $u_0 = U(\eta)/U_s$. Then, $\omega = \Omega/\tau = \Omega\gamma S_s/l$, where Ω is the dimensionless frequency. The complex frequency $\Omega = \Omega' + i\Omega''$ can be determined by solving these equations. A positive imaginary part $\Omega'' > 0$ corresponds to instability.

It is instructive to introduce the current perturbation $w = u_0 v_1 + u_1 v_0$. With the help of a simple relationship $v_0 = (M_s M^2)^{1/3}$ specified by Eq.(6), Eq.(10) can be re-written as follows:

$$w''\phi(M) + w'\frac{\gamma M}{s} \left(2i\Omega - \frac{1+2M^2}{\phi(M)} \right) + \quad (11)$$

$$w\frac{\Omega\gamma^2}{s^2} \left(\Omega + i\frac{1+M^2}{\phi(M)} \right) = 0, \\ w'(0) = 0, w(1) = 0, \quad (12)$$

We remind that the scale of the steady state nonuniformity is the channel length. The wavelengths of the lower-order modes of the plasma oscillations are on the same order of magnitude. In contrast, the higher-order modes have a considerably shorter scale. As stated in Ref.[4], the higher modes are more sensitive to the steady

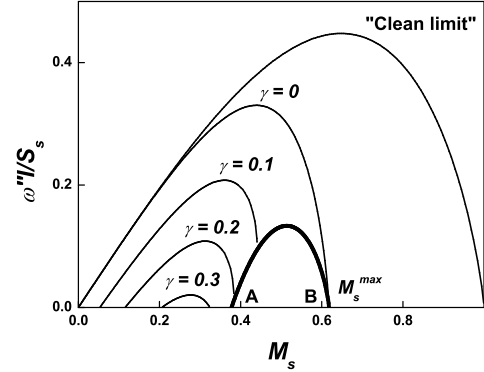


FIG. 2: Dimensionless increment of instability $\omega''l/S_s$ vs Mach number at the source for the: "clean limit" [1] at $p; \gamma = 0$, 2DEG with DVS($p = 1$) and different values of the friction parameter $\gamma = 0; 0.1; 0.2; 0.3$. The bold line A-B shows the increment of instability in the saturation mode (represented by A-B line in Fig.3). The point B corresponds to $M_s^{max}(1) = 0.62$.

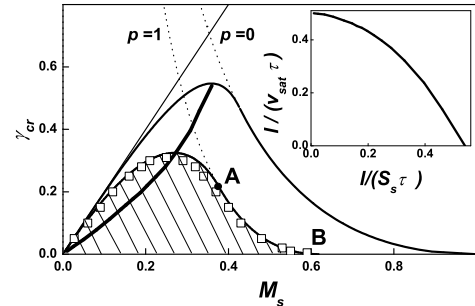


FIG. 3: Diagram of instability threshold. The critical value of the friction parameter, γ_{cr} vs Mach number at source (bold lines) and saturation threshold γ_{sat} (dotted lines) for $p = 0$ (see Ref.[4]) and $p = 1$. The thin line is the asymptote $\gamma_{cr} = 2M_s$. The increment of instability along the line A-B is shown in Fig.2. The point B corresponds to $M_s^{max}(1) = 0.62$. The ultra-bold line represents the maximum of the instability threshold $\gamma_{max}(M_s)$ for $0 < p < \infty$. The data obtained by numerical simulations based on Eqs.(1,2) are shown by squares. Inset: FET parameters γ vs γ^* required for plasma wave generation.

state nonuniformity than the fundamental and low-order modes. Since the increment of instability is strongly affected by the boundary-reflection coefficients, it would be expected that the higher-order modes are amplified more effectively. Based on such a qualitative argumentation, we analyze Eq.(11) within the higher-order mode approximation.

The spatial dependence of the Mach number $M(\eta)$ is

a monotonous function of the coordinate. Consequently, we can represent the current perturbation w as a function of the Mach number $w = w(M)$. Moreover, following Ref.[4] we search for the solution in the form $w = F \exp(g)$, where $g = -\frac{2}{3}(i\Omega + 5/4) \ln(M)$. Finally, we use Eq.(6) and, then, change the independent variable from η to M , to rewrite Eq.(11) as follows:

$$\frac{9}{4}M^4 F'' + \left[\Omega^2(1 - psM) + i\Omega + \frac{5}{16}M^2 \right] F = 0. \\ w'(M_s) = 0, w(M_d) = 0. \quad (13)$$

where we now denote by F', F'', w', w'' the derivatives with respect to M . It is noteworthy that Eq.(13) is exact. Solutions to this equation with given boundary conditions exist only for certain complex frequencies Ω (eigenvalues of the problem). Note the analogy between Eq.(13) and one-dimensional Schrödinger equation, in which the complex frequency Ω plays the role of energy in the quantum mechanics. In general, Eq.(13) can be solved only numerically. However, an analytical solution can be found using the high-order mode method [4] which corresponds to the quasi-classical approximation in quantum mechanics. This approach is valid when $|\Omega| \gg 1$, and, therefore, the imaginary part of Ω is small as compared with its real part, $\Omega' \gg \Omega''$. We now search for a solution to Eq.(13) in the form $F = \frac{A}{\sqrt{k}} \exp(-i \int k dM)$, where A is a constant, and $k(M)$ is the dimensionless wave vector. Finally, we obtain the dispersion equation as

$$k_{1,2} = \pm \frac{2}{3M^2} \left(\Omega \sqrt{1 - psM} + \frac{i}{2\sqrt{1 - psM}} \right). \quad (14)$$

Here we keep the main corrections with respect to powers of Ω , and, therefore, neglect the term $\frac{5}{16}M^2$ in Eq.(13). The wave vectors k_1, k_2 correspond to the plasma waves propagating down- and upstream, respectively. Searching the solution to Eq.(13) in the form $F = \sum_{l=1,2} \frac{A_l}{\sqrt{|k_l|}} \exp(-i \int k_l dM)$, with the given boundary conditions, we can easily find:

$$\exp \left(i \int_{M_s}^{M_d} (k_2 - k_1) dM \right) = R_s^I R_d^I \quad (15)$$

where $R_s^I = \frac{\sqrt{1 - psM} + M_s}{\sqrt{1 - psM} - M_s}$, $R_d^I = -1$ are the current amplitude reflection coefficients from the source and drain boundaries, respectively, and $R_s^I R_d^I$ is the round-trip gain factor. Eq.(15) allows finding of both the real and imaginary parts of Ω as follows:

$$\Omega'_n = \frac{3\pi n}{4} \frac{1}{\frac{(1 - psM)^{3/2}}{M} \Big|_{M_s}^{M_d}}, \quad (16)$$

$$\Omega'' = -\frac{\sqrt{1 - psM}}{2M} (1 + 2psM) \Big|_{M_s}^{M_d} + \frac{3}{4} \ln(R_s^I R_d^I). \quad (17)$$

We emphasize that, in the "clean limit" [1], i.e., at $\gamma; p = 0$, Eqs.(16,17) coincide with those specified by Eq.(4). Using of Eq.(17) and the relationship between the Mach numbers at the source and drain given by Eq.(8), we can easily obtain the dependence of the instability increment ω'' on Mach number at the source M_s for arbitrary friction γ and DVS strength p . Both the friction and the DVS effect result in instability damping (see Fig.2). Firstly, DVS leads to narrowing of the instability range. For example, at $p = 1$ and $\gamma = 0$ the instability exists within the range $0 < M_s < M_s^{max}(1) = 0.62$, which is narrower than that $0 < M_s < 1$ in the "clean limit". Secondly, at certain DVS strength the enhancement of friction suppresses the instability (see the curves for $p = 1$ in Fig.2). The region of instability narrows as well. Actually, in the case of $p = 1$ (Fig.2), the instability exists when $\gamma < 0.32$. This condition is more stringent as compared with the analogous $\gamma < 0.54$ in the absence ($p = 0$) of the DVS mechanism.

Substituting $\Omega'' = 0$ into Eq.(17) and using Eq.(8), we plot in Fig.3 the instability threshold $\gamma_{cr}(M_s, p)$ for two different DVS strengths $p = 0; 1$. In addition, the same figure shows by dotted lines the corresponding dependencies for the saturation threshold $\gamma_{sat}(M_s, p)$. At a certain point (denoted by "A" for the $p = 1$ case) both the threshold curves merge, and, thus give the threshold diagram of instability, marked by the shadowed area in Fig.3. The threshold diagram is confined between two asymptotes. One of these (thin line in Fig.3), given by $\gamma_{cr} = 2M_s$, is the same for both $p = 0$ and $p = 1$ cases. Actually, this is the result obtained previously in Ref.[1] for the case of a small friction, at which the spatial distribution of M is only slightly nonuniform. Then, the threshold diagram is bounded at high M_s by the saturation threshold curve $\gamma_{sat}(M_s, p)$. Note that, within a part of the latter asymptote (for the $p = 1$ case, the bold line A-B in Fig.3), the increment of instability is positive, as shown in Fig.2. In what follows, we explain the above discrepancy by the uncertainty of our high-order mode method.

Arguing that Fig.3 represents the instability threshold, we, in addition, determine γ_{cr} by numerical simulations based on Eqs.(1,2) and Eq.(3), using the previously described numerical method [2]. The results obtained (shown by squares in Fig.3) coincide with our theoretical curve within the error of the numerical method. As the numerical simulations give the threshold for the most unstable modes, this coincidence with the analytically obtained results, clearly demonstrates the validity of our approach.

We now present our central result, concerning the device parameters required for a possible observation of the instability. First, for certain p we find the maximum of the instability threshold $\gamma_{max}(p)$ (the corresponding dependence $\gamma_{max}(M_s)$ is represented by the ultra-bold line in Fig.3). Then, the general instability condition reads

$\gamma < \gamma_{max}(p)$. It will be recalled that $p = \frac{\gamma^*}{\gamma}$, where we introduce the dimensionless parameter $\gamma^* = \frac{l}{v_{sat}\tau}$ related to the DVS effect. With the above notation, the instability criterion yields

$$\gamma^* > \gamma_{max}^{-1}(\gamma)\gamma, \quad (18)$$

where $\gamma_{max}^{-1}(x)$ is the inverse function. In the inset in Fig.3, we plot the diagram specified by Eq.(18). The values of the FET parameters, confined by the bold curve, correspond to an instability. Another condition is related to the applicability of the hydrodynamic model suggested in Ref.[1]. In actual fact, 2D electrons can be considered a fluid when the mean free path $\lambda \sim \sqrt{N}$, associated with electron-electron collisions, is shorter than the channel length. This requirement can be easily transformed to $\gamma < \frac{l^2}{\mu} \sqrt{C/m}$.

The final question remaining to be resolved is whether the finite scattering and the DVS effect can influence the proper and the higher-order-mode frequencies of the instability. With the help of Eq.(16), we calculate the nth-order-mode frequency $\omega'_n(M_s, p, \gamma)$. At a fixed $p = 1$ in Fig.1, we plot the shadowed area (which corresponds to that in Fig.3) which shows all the possible plasma frequencies when the instability increment is positive $\Omega'' > 0$. At a fixed current $j \sim M_s$ and a finite p , the proper frequency and its harmonics may be much lower than those expected in "clean limit" (see Eq.(4)). The difference between two cases becomes more pronounced in the saturation mode, at $M_s \leq M_s^{max}$. We conclude that the DVS effect results in a strong depression of the plasma wave generation frequency.

We are now going to justify the applicability of the high-order-mode approach[4], developed in the present paper. We first compare the data presented in Figs.1,2, and, then conclude that our basic assumption $\Omega' > \Omega''$ is, surprisingly, valid for the proper plasma wave mode $n = 1$ as well. This is, however, not the case in the saturation mode, at $\Omega \rightarrow 0$, which seems to be the reason for a minor deviation between the theory and the results of our numerical simulations (see threshold diagram in Fig.3).

Let us represent the instability threshold shown in Fig.3 in current-voltage(I-V) plane of the transistor. In terms of the Mach number formalism, the current and the source-drain voltage swing yield

$$\frac{j}{j_0} = \gamma^{-3} M_s, \frac{U_{sd}}{U_0} = \gamma^{-2} (1 - (M_s/M_d)^{2/3}), \quad (19)$$

where we use the units $j_0 = WCm(l/\tau)^3/e$ and $U_0 = m(l/\tau)^2/e$, introduced in Ref. [14]. For a fixed M_s, γ, p , we can calculate M_d specified by Eq.(8) and then use Eq.(19) to find the steady-state I-V characteristics $j(U_{sd})$. In Fig.4 we plot I-V characteristic for certain values $p = 0; 1$. In addition, the instability threshold curves $\gamma_{cr}(M_s, p)$ can be transformed to those $j_{cr}(U_{sd})$

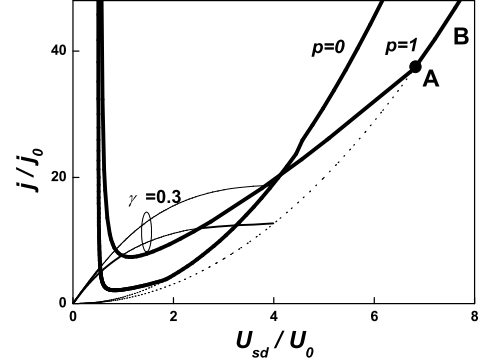


FIG. 4: Instability region in the I-V characteristic. The I-V curves are plotted for $\gamma = 0.3$, where the upper(lower) curve corresponds to $p = 0$ and $p = 1$, respectively. For $p = 0$ and $p = 1$ cases the bold (dotted) line (corresponding to those in Fig.3) indicates the instability (saturation) threshold respectively. The unstable parts of the current-voltage characteristics are indicated by thin lines. The line A-B corresponds to that shown in Fig.3

in the I-V plane. Furthermore, the dotted curves (corresponding to $\gamma_{sat}(M_s, p)$ in Fig.3) relate the saturation current to saturation source-drain voltage. For the $p = 1$ case, both the threshold curves, which merge at point A, confine the instability region in the I-V plane. The parts of the current-voltage characteristics lying within this region correspond to unstable states (thin lines in Fig.4). For $\gamma > 0.32(p = 1)$ and $\gamma > 0.54(p = 0)$, the current-voltage characteristics are always stable. Note that the saturation current at finite p is lower than that in absence of the DVS effect.

Theory vs experiment

We now provide a detailed analysis of the data obtained in a THz-emission experiment[12] for an ultrashort-channel InGaAs-based FET. In this device, the source-drain separation of $1.3\mu\text{m}$ was made much longer than the gate length $l = 60\text{nm}$. Thus, the total series resistance R associated with the gate-source and gate-drain access regions may affect the I-V characteristics of the device. Indeed, the voltage bias between the source and drain ends of the gated part of the channel U_{sd} is related to the external (hereafter marked by prime) source-to-drain terminal voltage by $U'_{sd} = U_{sd} + jR$. Then, for the actual case of a symmetric FET (see inset in Fig.5) the swing voltage U_s is related to the external gate-to-source voltage by $U_s = U'_{gs} - U_T - jR/2$. We further use the simplest channel pinch-off model, for which the I-V dependence of the device is given by $j = \beta U_{sd}(U_s - U_{sd}/2)$, where $\beta = WC\mu/l$ is the I-

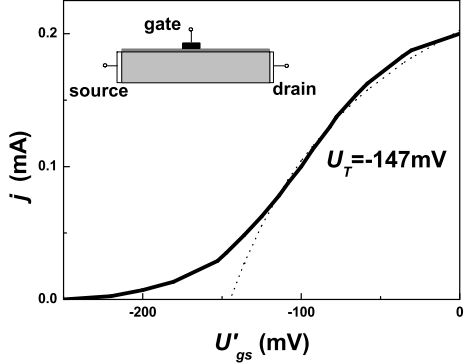


FIG. 5: I-V transfer characteristic (bold line) at $U'_{sd} = 5\text{mV}$, reproduced from Ref.[12]. Dotted line represents the fit with Eq.(20). Inset: schematic of the short-channel FET.

V steepness. Assuming that the actually measured I-V characteristic is expressed in terms of terminal voltages U'_{gs} , U'_{sd} , we derive I-V dependence as follows

$$j = \beta \frac{U'_{sd}(U'_s - U'_{sd}/2)}{1 + \beta R(U'_s - U'_{sd}/2)}. \quad (20)$$

where $U'_s = U'_{gs} - U_T$. We now analyze the I-V transfer characteristics measured[12] at a fixed source-drain bias $U'_{sd} = 5\text{mV}$. According to Eq.(20), if the applied gate-to-source terminal voltage U'_{gs} exceeds a certain threshold value $U_T + U'_{sd}/2$, the current is nonzero. Then, at high U'_{gs} , the current saturates, being limited only by the only series resistance, and, hence $j = U'_{sd}/R$. In Fig.5, we reproduce the observed FET transfer characteristic (see inset in Fig.1 of [12]) and then put on the same plot our best-fit data. Note that Eq.(20) is, in fact, valid only in the gradual Shockley approximation, and, therefore, the subthreshold mode $U'_{gs} - U_T < 0$ is not analyzed in Fig.5. The device parameters obtained are as follows: $\beta = 0.66 \frac{1}{\Omega V}$, $R = 14\Omega$, and $U_T = -147\text{mV}$. For $\epsilon = 12.7$, gate-to-channel separation $d = 17\text{nm}$, and gate width $W = 50\mu\text{m}$, the FET mobility is $\mu = 1200\text{cm}^2/\text{Vs}$. The corresponding momentum relaxation time is $\tau = 2.9 \times 10^{-14}\text{s}$.

The next step of our analysis is concerned the FET I-V characteristic [12] at a fixed gate-to-source voltage (in the experiment $U'_{gs} = 0$, and, therefore, $U'_s = -U_T$). At a fixed U'_s the current is linear in the source-to-drain bias $j = \frac{U'_{sd}}{R_{ch} + R}$, where $R_{ch} = (\beta U'_s)^{-1}$ denotes the channel resistance. At a certain source-to-drain bias, the device current saturates (channel pinch-off) when $dj/dU'_{sd} = 0$. Both the saturation current and voltage are given by

$$j_{sat} = 2\beta(U'_s)^2 \left(\frac{\sqrt{1+r} - 1}{r} \right)^2,$$

TABLE I: Experiment vs theory

2DEG	$l d$, nm	R , Ω	U_T , V	μ , $\frac{\text{cm}^2}{\text{Vs}}$	$S_s V_{sat}$, $\times 10^5 \frac{\text{m}}{\text{s}}$	$\gamma \gamma^*$
InGaAs[12]	60 17	14	-0.147	1200	7.0 3.2	3.0 6.6
$m^* = 0.042$						
GaN[12]	1500 25	62	-2.8	1700	11.3 3.5	6.3 20
$m^* = 0.22$						

$$U'_{sd}|^{sat} = 2U'_s \frac{1 + r - \sqrt{1 + r}}{r}, \quad (21)$$

where $r = R/R_{ch}$. Without the series resistance R , Eq.(21) reproduces the conventional channel pinch-off saturation at $j_{sat} = \beta U_s^2/2$, $U_{sd}^{sat} = U_s$. By contrast, at a nonzero R , the saturation current decreases and the saturation voltage increases as compared with the $R = 0$ case. For the I-V characteristic reported in [12], we have $U'_s = 147\text{mV}$, and, therefore, the channel resistance is $R_{ch} = 11\Omega$. The total resistance $R + R_{ch} = 14 + 11 = 25$ is comparable with the value of 29Ω , obtained in [12] from the linear part of the I-V curve. Then, we estimate both the saturation current $j_{sat} = 4.4\text{mA}$ and voltage $U'_{sd}|^{sat} = 180\text{mV}$, which are, however, somewhat low than those obtained in the experiment.

We now discuss the most intriguing result[12] concerning the irradiation $f \sim 0.4\text{THz}$, observed at certain current $j = 4.5\text{mA}$ and voltage $U'_{sd} = 200\text{mV}$. The above emission threshold corresponds to $U_{sd} = U'_{sd} - jR = 70\text{mV}$ and effective voltage swing $U_s = U'_{gs} - U_T - jR/2 = 116\text{mV}$. In contrast to Ref.[12], we conclude that the observed emission threshold precedes the saturation mode of the transistor because $U_{sd} < U_s$. Our conclusion can be further confirmed by analyzing the actual shape of the I-V characteristic reported in Ref.[12]. In general, the output drain conductance vanishes in the saturation mode, i.e. $\frac{dj}{dU'_{sd}} = 0$, irrespective of the actual mechanism (channel pinch-off, DVS mechanism based on smooth $\tau(E)$ dependence, "chocking"). Obviously, this is not the case for the THz-emission threshold point reported in Ref.[12].

We now verify whether the device parameters γ, γ^* match the limits(see Fig.4, inset) required for plasma wave instability to occur. For $m = 0.042m_0$, we find the plasma wave velocity $S_s = \sqrt{eU_s/m} = 7.0 \times 10^5 \text{m/s}$ and the 2D density $N_s = \frac{\epsilon_0 \epsilon U_s}{de} = 3.5 \times 10^{11} \text{cm}^{-2}$. We estimate the friction strength as $\gamma = \frac{l}{S_s \tau} = 3.0$. Then, with the textbook value for the saturation velocity $V_{sat} = 3.2 \times 10^5 \text{m/s}$, we obtain $p = 2.2$, hence $\gamma^* = 6.6$. Both the parameters γ, γ^* exceed the limits (see Fig.4, inset) required for instability. Hence, the observed sub-THz emission [12] cannot be attributed to the plasma wave instability scenario. Moreover, our step-by-step analysis (see Table 1) of the data for a $1.5\mu\text{m}$ -channel GaN FET[12] shows that the GHz-emission ob-

served does not originate from the "shallow-water" mechanism, either.

Conclusion

We have shown that both the scattering and the DVS effect depress the frequency and the instability increment. The experimental results reported in Refs.[12],[12] for sub-THz emission in ultra-short channel FETs cannot be explained in terms of the plasma instability scenario[1].

This study was supported by Large Scale Facility program (Weizmann Institute, Israel, grant No.HPRI-CT-2001-00114) and Russian Foundation for Basic Research (grant No.03-02-17588).

- [1] M.Dyakonov and M.Shur, Phys.Rev.Lett. **71**, 2465 (1993)
- [2] A.P.Dmitriev, A.S.Furman, V.Yu.Kachorovskii, G.G.Samsonidze, and Ge.G.Samsonidze, Phys.Rev.B **55**, 10319 (1997)
- [3] M.V.Cheremisin, Phys.Rev B **65**, 085301 (2002)
- [4] M.V.Cheremisin, M.I.Dyakonov, M.Shur, and G.G.Samsonodze, Sol.State Electr. **42**, 1737 (1998)

- [5] M.Dyakonov and M.Shur, IEEE Trans. Electron Devices **43**, 380 (1996)
- [6] J.-Q. L and M.S.Shur, Appl. Phys. Lett., **78**, 2587 (2001)
- [7] W.Knap, V.Kachorovskii, Y.Deng, S.Rumyantsev, J.-Q.L, R.Gaska, M.S.Shur, G.Simin, X.Hu, M.Asif Khan, C.A.Saylor, and L.C.Brunel, J. Appl. Phys. **91**, 9346 (2002)
- [8] W.Knap, Y.Deng, S.Rumyantsev, J.-Q.L, M.S.Shur, C.A.Saylor, and L.C.Brunel, Appl. Phys. Lett., **80**, 3433 (2002)
- [9] W.Knap, Y.Deng, S.Rumyantsev, and M.S.Shur, Appl. Phys. Lett., **80**, 4637 (2002)
- [10] W.Knap, F.Teppe, Y.Meziani, N.Dyakonova, J.Lusakowski, F.Boeuf, T.Skotnicki, D.Maude, S.Rumyantsev and M.Shur, Appl. Phys. Lett., **85**, 675 (2004)
- [11] X.G.Peralta, S.J.Allen, M.C.Wanke, N.E.Narff, J.A.Simmons, M.P.Lilly, J.L.Reno, P.J.Burke, and J.P.Eisenstein, Appl. Phys. Lett., **81**, 1627 (2002)
- [12] W.Knap, J.Lusakowski, T.Parenty, S.Bollaert, A.Cappy, V.V.Popov, and M.S.Shur, Appl.Phys.Lett. **84**, 2331 (2004)
- [13] Y.Deng, R.Kersting, J.Xu, R.Ascazubi, Xi-Cheng Zhang, M.S.Shur, R.Gaska, G.S.Simin, M.Asif Khan and V.Ryzhii, Appl.Phys.Lett. **84**, 70 (2004)
- [14] M.Dyakonov and M.Shur, Phys.Rev.B **51**, 14341 (1995)
- [15] M.V.Cheremisin, Semiconductors **31**, 241 (1997)